IEEE Access®
Multidisciplinary : Rapid Review : Open Access Journal

Modeling of a Droop-Controlled Grid-Connected DFIG Wind Turbine

I. ORAA, (Student Member, IEEE), J. SAMANES, (Member, IEEE), J. LOPEZ, (Member, IEEE), and E. GUBIA, (Member, IEEE)

[1]Department of Electrical, Electronic and Communications Engineering, Public University of Navarre (UPNA), Campus de Arrosadia 31006 Pamplona, Spain
[2]Institute of Smart Cities (ISC), Public University of Navarre (UPNA), Campus de Arrosadia 31006 Pamplona, Spain

Corresponding author: I. Oraa (e-mail: iker.oraa@unavarra.es).

ABSTRACT Traditionally, to characterize the response of droop-controlled systems RMS models have been used. However, as it is demonstrated in this work, when droop control is applied to doubly-fed induction generators, RMS models do not allow to predict the system stability and dynamic response. Thus, in this article a linearized small-signal model that overcomes the limitations of RMS models is presented. The proposed model is validated by simulation in MATLAB/Simulink demonstrating that it allows to accurately analyze the stability and dynamic response of the system under study. This model is an interesting tool that can be used in future works to design and adjust grid-forming controllers for doubly-fed induction generators.

INDEX TERMS Doubly-Fed Induction Generator (DFIG), Droop Control, Small-Signal Modeling.

I. INTRODUCTION

Currently the control of power grids falls mainly on synchronous generators (SG) of large conventional fossil-fuel power plants. However, there are ambitious global targets in the field of environmental and energy policies to reduce the use of fossil fuels by replacing them with renewable energies (RREE) such as wind power. Today, wind power is, together with photovoltaic, the main renewable energy and it is called to play a fundamental role in this energy transition process.

Doubly-fed induction generators (DFIG) dominate the variable speed onshore wind turbine market [1]. As SGs are replaced by RREE, such as DFIG wind turbines, there is a risk that the stability of the grid will be compromised as the grid-following (GFL) control strategies implemented in most power converters require the presence of a strong grid, where frequency and voltage are imposed by SG. Therefore, it is necessary to implement controls that contribute to guarantee the stability of the electrical grid. This way, in recent years, the research community has focused on developing grid-forming (GFM) control strategies that allow to solve the challenges involved in the large-scale integration of RREE, to ensure a stable and safe operation of the power system [2], [3].

Power converters based on GFM control strategies behave as voltage sources that inject power into the grid imposing both the voltage amplitude and frequency. The power con-

verter maintains these parameters within predefined limits, helping to ensure grid stability. Unlike GFL control, GFM control systems do not require an existing power grid to operate. In this sense, it is possible to implement a control in an isolated system so that it is the converter itself that creates and imposes the voltage and frequency characteristics to all loads connected to it such as in the case of grid black-outs. Among multiple GFM control strategies droop control [4], [5], virtual synchronous machine control (VSM) [6], [7], machine matching control [8], virtual oscillator control (VOC) [9], [10] and dispatchable virtual oscillator control (dVOC) [11], [12] stand out.

Droop control is used in the parallel operation of power converters to ensure proper load sharing among the different generating units [13], [14]. Power converters based on this control strategy act as voltage sources, allowing to regulate the active and reactive power output. The control consists of two droop control loops, an active power-frequency control loop (P-f) and another reactive power-voltage control loop (Q-V), which adjust the phase angle and amplitude of the voltage imposed by the converter respectively. In the Q-V control loop a PI controller is usually implemented to ensure reactive power reference tracking, while in the P-f control loop a proportional controller is sufficient to track active power references. Regarding grid synchronization method, droop control structures do not require the use of an ad-

ditional unit, such as a phase locked loop (PLL), for synchronization purposes during normal operation [5], [7], [15], [16]. This allows power converters to form an AC grid and to operate whatever the grid-topology, unlike GFL power converters that operate only in a grid-connected mode and need grid information to be synchronized. However, although a dedicated synchronization unit is not necessary for normal operation, in some droop control structures a back-up PLL is employed for pre-synchronization purposes, as well as for operation during grid faults [13].

Droop control has been widely studied and has been mainly applied to grid-connected power converters [5], [17]–[27]. When analyzing the response of these systems, RMS models are commonly used. In these models, it is assumed that the inductive component of the network impedance is much larger than the resistive component, which typically happens in high and medium voltage lines. Thus, the resistive component of the grid impedance is neglected, and it is assumed that the angle between the voltage applied by the converter and the grid voltage, called load angle, is small [21], [23], [26], [27]. In addition to RMS models, some authors [19], [20], [24], [25] employ small-signal state-space models to characterize the power converters line dynamics and analyze the eigenvalues of the system. However, the use of RMS models is more widespread due to their greater simplicity, in comparison with small-signal models, and good performance when characterizing the behavior of grid-connected power converters.

Droop control has also been applied to DFIG wind turbines, but the studies carried out are not very numerous at the moment [28]–[37]. In almost all case studies, in addition to droop control loops, inner current and/or voltage loops are implemented. Thus, some authors [29], [31]–[33], [35] assume that the DFIG acts as a controllable voltage source and they use the usual RMS models to characterize the power exchange with the grid, without taking into account the internal dynamics of the machine. Other authors do model the internal dynamics of the machine, even if they implement inner current and/or voltage loops [37], [38]. In [37] a droop control with inner voltage and current loops is implemented and a transfer matrix based impedance model is developed to analyze stability and to study the influence of the control structure and short circuit ratio. Likewise, in [38] a GFM control with an inner voltage loop is implemented and a transfer matrix based impedance modeling process is presented in detail. In both papers the internal dynamics of the DFIG are modeled, but the nonlinearities that the system presents, due to the interaction of the machine with the control, are not fully considered. The P-f control loop adjust the angular frequency, ω, so the model depends on a variable ω, but in [37], [38] ω is assumed to be constant.

Although the work done so far for DFIG wind turbines has focused on the implementation of droop control with inner current and/or voltage loops, these inner control loops can be eliminated, what allows to resemble the droop control to the control of a SG [24]. With no inner loops the control

structure is simpler, and the dynamic response and small-signal stability improve [26]. However, with the absence of inner current and voltage control loops the machine dynamics become more relevant, which requires the correct modeling of the DFIG and its interaction with the droop control. In this article, in order to fully model the machine and its interaction with the control, first, a RMS model, as those generally used in grid-connected power converters, is employed. However, when analyzing the stability and dynamic response of the system, it is verified that the RMS model do not allow to predict the system stability and dynamics. Thus, a small-signal model, that takes into account all the nonlinearities that the system presents due to the interaction between the machine and the implemented control, is proposed. This model is validated by simulation in MATLAB/Simulink, proving that it allows to analyze the stability and to reproduce the dynamic response of the system under study accurately, unlike the models developed in previous works.

II. SYSTEM DESCRIPTION

The system under study shown in Fig. 1 consists of a grid-connected DFIG wind turbine. The rotor-side converter (RSC) is directly connected to the rotor and controls the torque and rotational speed of the generator. The grid-side converter (GSC) controls its output current, i_{gsc}, to regulate the DC bus voltage, v_{DC}, and it is connected to the stator terminals through the output inductance L_{GSC}. The grid is modeled as an ideal voltage source, v_g, with a series inductance, L_g. Even though the system shown in Fig. 1 represents a single grid-connected DFIG wind turbine, it could also represent an aggregate set of N number of DFIG wind turbines with the same parameters that operate under the same conditions. In this case, it would be necessary to multiply the grid inductance by the number of wind turbines connected in parallel to the point of common coupling (PCC), N, as it is explained in [39]. The voltage v_s represents the stator voltage, and the currents i_s, i_r, and i_g the stator, rotor, and grid currents respectively.

The DFIG is controlled in the synchronous reference frame or $d - q$ axes. In the GSC a conventional current control is applied, while in the RSC a droop control without PLL is implemented. The droop control structure is detailed in Fig. 1. On the one hand, the reactive power-voltage control loop adjusts the voltage amplitude imposed by the RSC on the rotor. The PI regulator of the Q-V control loop provides an increase in the rotor voltage amplitude, ΔV_r, depending on the difference between the reference reactive power, $Q_{s,ref}$, and the reactive power measured at the stator, $Q_{s,meas}$. This increment is added to the voltage reference, $V_{r,ref}$, and the reference voltage, aligned with the d axis, $V_{rd,ref}$, is obtained. On the other hand, the active power-frequency control loop regulates the frequency and phase of the rotor voltage so that the use of a PLL for synchronizing the RSC with the grid is not required. The P-f control loop provides an increase in the voltage frequency imposed by the RSC, $\Delta\omega$, proportional to the defined P-f droop coeffi-
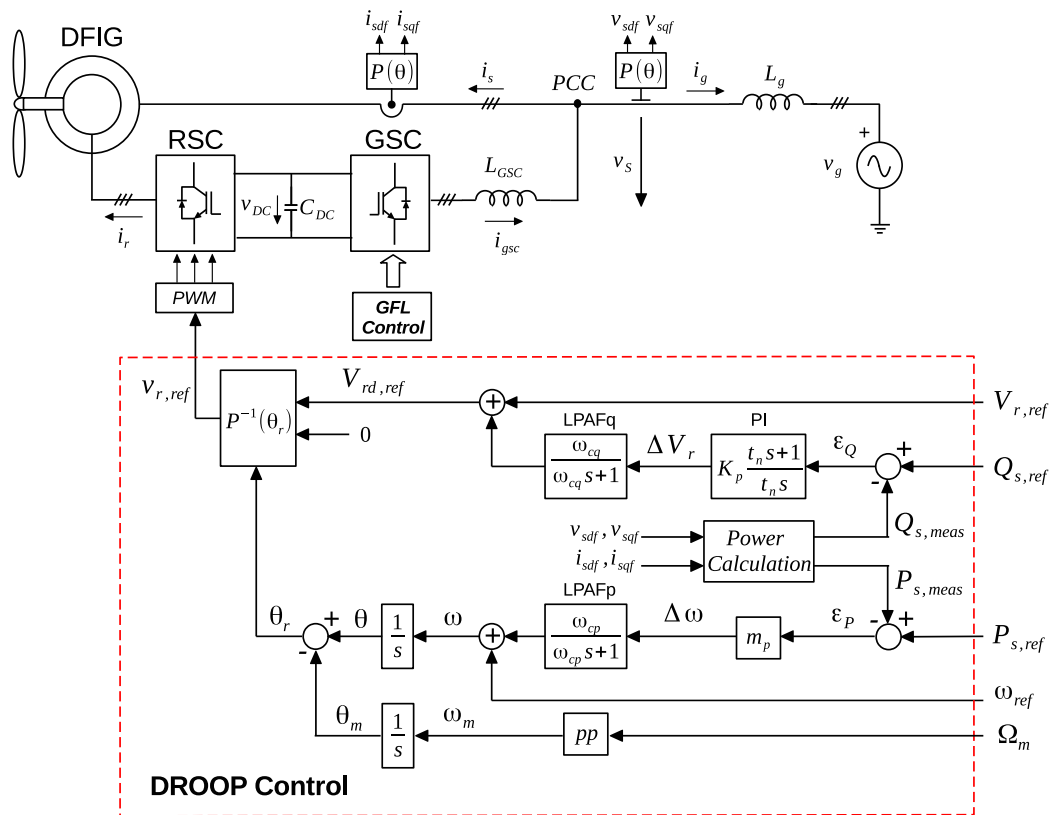
FIGURE 1. Droop control for a DFIG wind turbine.

cient, m_p, and to the difference between the reference active power, $P_{s,ref}$, and the measured active power, $P_{s,meas}$. This increment is added to the frequency reference, ω_{ref}, and the frequency ω is obtained. Integrating ω, the angle θ, which is used for the application of Park transformation of the stator variables, is obtained. Thus, the filtered measurements of the stator voltages and currents in the $d-q$ axes, v_{sdf}, v_{sqf}, i_{sdf} and i_{sqf}, are obtained, and from this measurements the stator active and reactive powers are calculated. The angle required for the application of Park transformation of the rotor variables and, in this case, for obtaining the three-phase rotor reference voltage in real magnitude, $v_{r,ref}$, depends on the position of the rotor, θ_m, which, in turn, depends on the rotational speed of the machine Ω_m. Both loops include a low-pass analog filter, $LPAF_p$ and $LPAF_q$, where ω_{cp} and ω_{cq} are the cut-off frequencies of the active and reactive power filters respectively.

In the system modeling presented below, the subscripts s, r and g refer to the stator, rotor, and grid variables respectively, and the subscripts d and q to the d and q axes. When modeling the system, a small-signal analysis is performed so that the state variables are defined as $x = X_0 + \Delta X$, where x is the state variable, X_0 is the steady-state value, and ΔX is a small-signal perturbation. It should be noted that the GSC has little influence on small-signal stability, so when modeling the system its analysis will be neglected as in [38].

III. LIMITATIONS OF RMS MODELS FOR DROOP-CONTROLLED DFIG WIND TURBINES

A. SIMPLIFIED RMS MODEL

In this section, following the dominant methodology in the literature, an RMS model is developed to analyze the power exchange between two voltage sources; the droop-controlled RSC and the grid. In the implemented droop control, since there are no inner current or voltage control loops, the control directly adjusts the voltage at the RSC output terminals, so the influence of the DFIG and the grid impedance must be considered when modeling the exchanged power [26]. Fig. 2 (a) shows the equivalent circuit from which the RMS model is developed. The circuit includes the DFIG steady-state equivalent circuit, referred to the stator, and the grid-connection impedance, where R_s and R_r are the stator and rotor resistors, X_l and X_0 are the equivalent leakage reactance and the magnetization reactance of the machine. I_0 is the no-load current, s is the slip and X_g the grid reactance. The magnetic losses of the machine and the resistive component of the grid impedance are assumed to be negligible. The voltages and currents are represented in phasor form by the superscript '—'.

The grid current, $\bar{I}_g$, can be written as

$$\bar{I}_g = \bar{I}_r - \bar{I}_0 = \bar{I}_r - \frac{\bar{V}_s}{jX_0}. \tag{1}$$
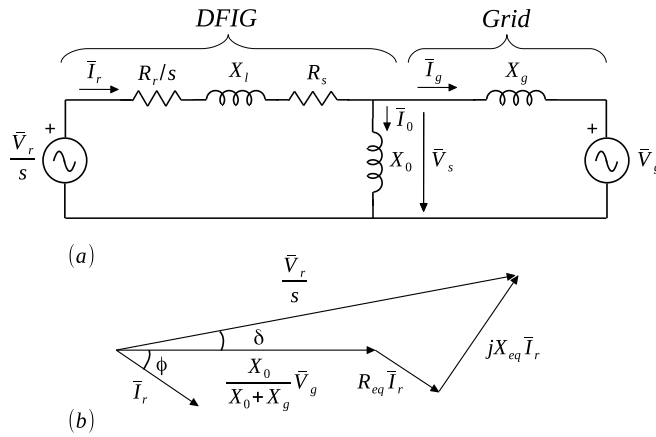
FIGURE 2. Simplified RMS model of a DFIG wind turbine connected to the grid: (a) equivalent circuit and (b) phasor diagram.

Then, the stator voltage, $\bar{V}_s$, can be expressed as

$$\bar{V}_s = \bar{V}_g + jX_g\bar{I}_g = \bar{V}_g + jX_g\left(\bar{I}_r - \frac{\bar{V}_s}{jX_0}\right). \quad (2)$$

Therefore,

$$\bar{V}_s = \frac{X_0}{X_0 + X_g}\bar{V}_g + j\frac{X_0X_g}{X_0 + X_g}\bar{I}_r. \quad (3)$$

The voltage applied in the rotor by the RSC can be expressed as

$$\frac{\bar{V}_r}{s} = \bar{V}_s + \left(\frac{R_r}{s} + R_s + jX_l\right)\bar{I}_r. \quad (4)$$

Substituting (3) into (4), the following equation is obtained

$$\frac{\bar{V}_r}{s} = \frac{X_0}{X_0 + X_g}\bar{V}_g + \left[\frac{R_r}{s} + R_s + j\left(X_l + \frac{X_0X_g}{X_0 + X_g}\right)\right]\bar{I}_r. \quad (5)$$

Defining the variables

$$R_{eq} = \frac{R_r}{s} + R_s, \quad (6)$$

$$X_{eq} = X_l + \frac{X_0X_g}{X_0 + X_g}, \quad (7)$$

$$Z_{eq}^2 = R_{eq}^2 + X_{eq}^2, \quad (8)$$

and

$$a = 3\frac{\frac{X_0}{X_0 + X_g}V_g}{Z_{eq}^2}, \quad (9)$$

the voltage applied by the RSC can be compactly written as

$$\frac{\bar{V}_r}{s} = \frac{X_0}{X_0 + X_g}\bar{V}_g + (R_{eq} + jX_{eq})\bar{I}_r. \quad (10)$$

The expression (10) can be represented in a phasor diagram as the one shown in Fig. 2 (b). From this phasor diagram the expressions of the active (P_g) and reactive (Q_g) powers injected to the grid are obtained

$$P_g = aR_{eq}\left(\frac{V_r}{s}cos\delta - \frac{aZ_{eq}^2}{3}\right) + aX_{eq}\frac{V_r}{s}sin\delta, \quad (11)$$

$$Q_g = -aR_{eq}\frac{V_r}{s}sin\delta + aX_{eq}\left(\frac{V_r}{s}cos\delta - \frac{aZ_{eq}^2}{3}\right). \quad (12)$$

The above expressions are not linear as the load angle δ and the voltage applied in the rotor by the RSC, V_r, are adjusted by the control loops, and thus are variable. In this case, unlike the usual RMS models [21], [23], [26], [27], the angle δ cannot be assumed to be small since the inductance of the grid-connection impedance is added to the inductance of the machine that can be greater than 0.3 pu. Therefore, a small-signal model should be used to linearize these expressions around an operating point. Defining the angle δ and the voltage V_r as

$$\delta = \delta_0 + \Delta\delta,$$

$$V_r = V_{r0} + \Delta V_r,$$

and developing (11) and (12), the linearized power expressions are obtained

$$\Delta P_g = \frac{aR_{eq}}{s}(-V_{r0}sin\delta_0\Delta\delta + cos\delta_0\Delta V_r) + \\ + \frac{aX_{eq}}{s}(V_{r0}cos\delta_0\Delta\delta + sin\delta_0\Delta V_r), \quad (13)$$

$$\Delta Q_g = \frac{-aR_{eq}}{s}(V_{r0}cos\delta_0\Delta\delta + sin\delta_0\Delta V_r) + \\ + \frac{aX_{eq}}{s}(-V_{r0}sin\delta_0\Delta\delta + cos\delta_0\Delta V_r). \quad (14)$$

Equations (13) and (14) can be expressed in matrix form as

$$\begin{pmatrix} \Delta P_g \\ \Delta Q_g \end{pmatrix} = [PQ]\begin{pmatrix} \Delta\delta \\ \Delta V_r \end{pmatrix}, \quad (15)$$

where

$$[PQ] = \frac{a}{s}\begin{bmatrix} V_{r0}(-R_{eq}sin\delta_0 + X_{eq}cos\delta_0) & R_{eq}cos\delta_0 + X_{eq}sin\delta_0 \\ -V_{r0}(R_{eq}cos\delta_0 + X_{eq}sin\delta_0) & -R_{eq}sin\delta_0 + X_{eq}cos\delta_0 \end{bmatrix}. \quad (16)$$

The matrix $[PQ]$ relates the load angle, $\Delta\delta$, and the RMS value of the voltage imposed by the RSC, ΔV_r, which are

adjusted by the P-f and Q-V droop control loops, with the active and reactive powers injected into the grid, ΔP_g and ΔQ_g.

Fig. 3 depicts the RMS model in block diagram form. The block $D_{conv}(s)$ included in the control diagram models the delay of one sampling period due to the calculation time of the DSP and the effect of the zero-order hold, which represents the PWM converter. To model the effect of such delays, the first-order Padé approximation [39] is used

$$D_{conv}(s) = \frac{1 - 0.5sT_s}{(1 + 0.5sT_s)^2}. \tag{17}$$

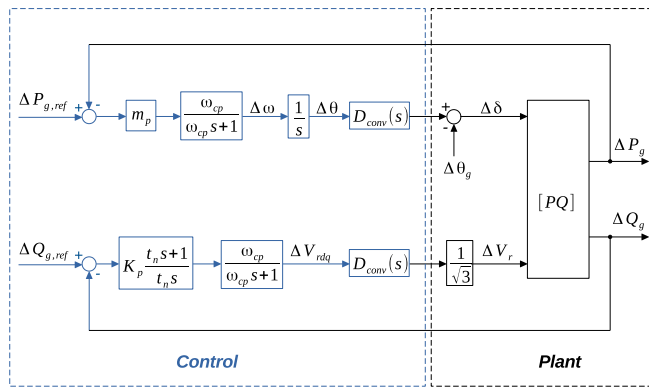FIGURE 4. Simulink and RMS model stability comparison.

FIGURE 3. RMS model block diagram.

B. MODEL VALIDATION

In order to test the validity of the RMS model, a model of the system under study has been built in MATLAB/Simulink. The system parameters are specified in Appendix A, where all parameters of the DFIG are referred to the stator. The model has been built with blocks from the Simscape / Electrical / Specialized Power Systems library. For the DFIG the Asynchronous Machine block is used. This block implements a three-phase asynchronous machine whose electrical part is represented by a fourth-order state-space model, and the mechanical part by a second-order system [40], [41]. The Simulink model is taken as reference for the validation of the developed RMS model. To determine the stability of the Simulink model, its response across the operating speed range of the machine has been simulated, in this case from 1050 to 1950 rpm, since the operation is limited to a slip of $\pm 30\%$. A step from 1.8 MW to 2 MW has been introduced in the reference active power, keeping the reference reactive power at zero, and the response has been analyzed. The stability results obtained in the simulations are graphically represented in the first column of Fig. 4.

Similarly, the stability of the RMS model represented in Fig. 3 has been analyzed in MATLAB. Once the model has been implemented, it has been linearized for an active power equal to 2 MW and a null reactive power, and the closed-loop poles of the system in the operating speed range of the
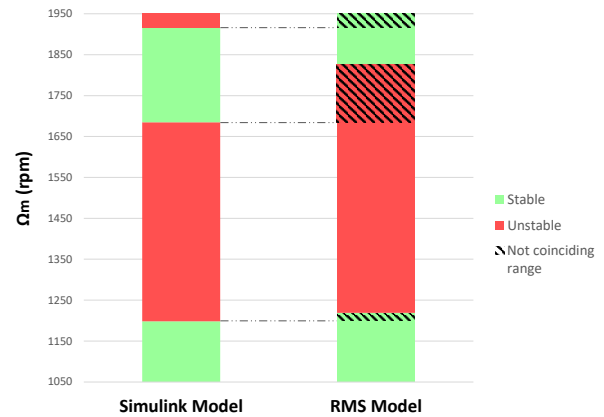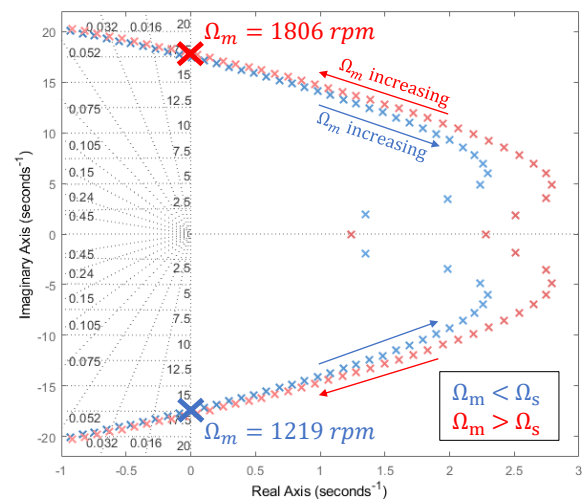

FIGURE 5. Evolution of the closed-loop poles of the RMS model as a function of rotational speed.

machine have been obtained. In Fig. 5 the evolution of the closed-loop poles as a function of the machine's rotational speed, Ω_m, is plotted. The poles corresponding to rotational speeds below the synchronous speed, Ω_s, are represented in blue and the poles corresponding to speeds above the synchronous speed are shown in red. This way, the stability range of the RMS model is determined (see second column of Fig. 4).

As can be seen in Fig. 4, the stability range of both models does not match. The Simulink model is stable from 1050 to 1198 rpm and from 1686 to 1917 rpm, while the RMS model is stable from 1050 to 1219 rpm and from 1806 to 1950 rpm.

In addition to the fact that the stability range of the models does not match, if their step-response is compared it can be seen that the RMS model does not allow to model the real dynamics of the system. In Fig. 6 the step-response of both models at 1050 rpm is represented, comparing the evolution of active and reactive power, and as can be seen the

RMS model does not reproduce the behavior of the Simulink model. Therefore, the RMS model cannot be considered a valid model to analyze the stability and dynamics of the system under study.
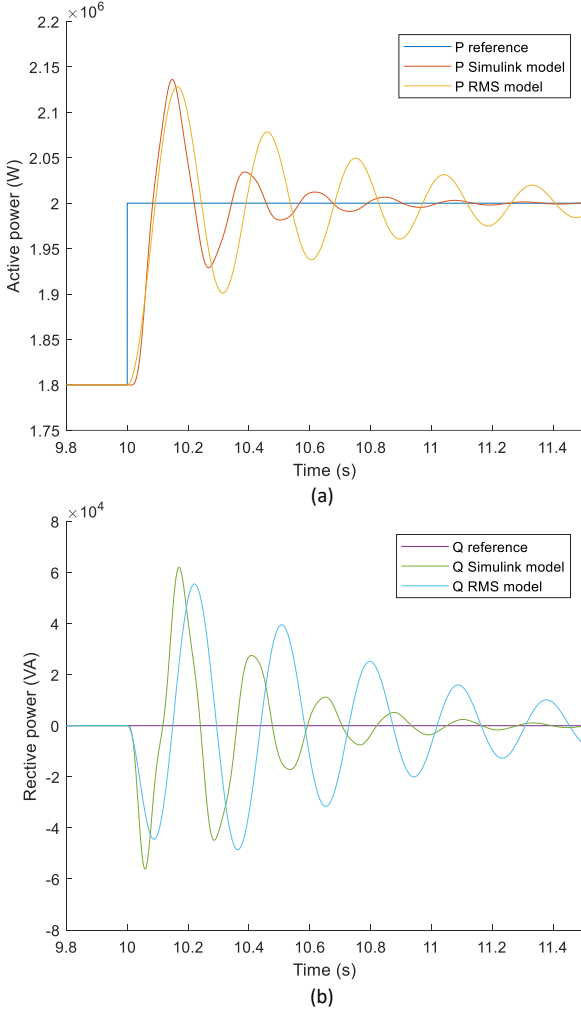

FIGURE 6. Step-response of Simulink and RMS model at Ω_m=1050 rpm: (a) active power and (b) reactive power.

IV. PROPOSED MODEL

In this section the small-signal model that overcomes the limitations of the RMS model is presented. First, the DFIG state-space model is developed to model the dynamics of the stator voltages and currents. Second, from these voltages and currents the stator active and reactive powers are calculated.

A. DFIG ANG GRID MODEL

Fig. 7 represents the DFIG equivalent circuit in the $d - q$ axes, where v_{sd}, v_{sq}, v_{rd} and v_{rq} are the stator and rotor voltages, i_{sd}, i_{sq}, i_{rd} and i_{rq} are the stator and rotor currents, ψ_{sd}, ψ_{sq}, ψ_{rd} and ψ_{rq} are the stator and rotor fluxes, L_{ls} and L_{lr} are the stator and rotor leakage inductances, L_m is the mutual inductance and ω and ω_m are the angular speed of

the $d - q$ reference and the electrical rotational speed of the machine, respectively. All DFIG variables and parameters are referred to the stator. The circuit includes the grid-connection impedance, where R_g represents the resistive component, L_g the inductive component, and ψ_{gd} and ψ_{gq} the grid flux.
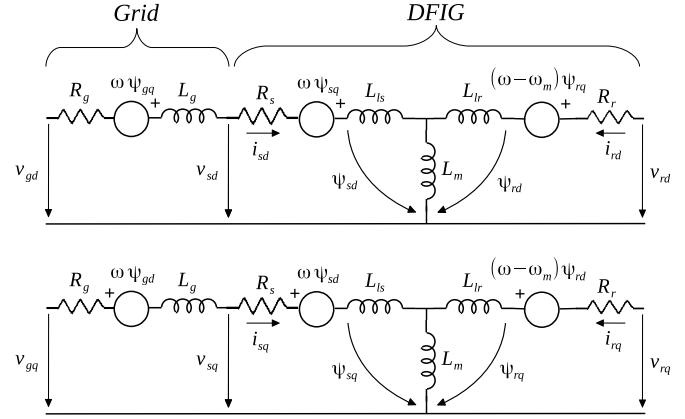

FIGURE 7. DFIG equivalent circuit in the $d - q$ axes.

The following differential equations define the DFIG model represented in Fig. 7

$$v_{gd} = R_{gs}i_{sd} + \frac{d\psi_{gsd}}{dt} - \omega\psi_{gsq}, \qquad (18)$$

$$v_{gq} = R_{gs}i_{sq} + \frac{d\psi_{gsq}}{dt} + \omega\psi_{gsd}, \qquad (19)$$

$$v_{rd} = R_r i_{rd} + \frac{di_{rd}}{dt} - (\omega - \omega_m)\psi_{rq}, \qquad (20)$$

$$v_{rd} = R_r i_{rq} + \frac{di_{rq}}{dt} + (\omega - \omega_m)\psi_{rd}, \qquad (21)$$

where

$$R_{gs} = R_g + R_s, \qquad (22)$$

$$\psi_{gsd} = \psi_{gd} + \psi_{sd} = L_{gs}i_{sd} + L_m i_{rd}, \qquad (23)$$

$$\psi_{gsq} = \psi_{gq} + \psi_{sq} = L_{gs}i_{sq} + L_m i_{rq}, \qquad (24)$$

$$\psi_{rd} = L_r i_{rd} + L_m i_{sd}, \qquad (25)$$

$$\psi_{rq} = L_r i_{rq} + L_m i_{sq}, \qquad (26)$$

where $L_{gs} = L_g + L_s$, $L_s = L_{fs} + L_m$, and $L_r = L_{fr} + L_m$.

Substituting (22)-(26) into (18)-(21), a system of four first-order differential equations is obtained

$$v_{gd} = R_{gs}i_{sd} + L_{gs}\frac{di_{sd}}{dt} + L_m\frac{di_{rd}}{dt} - \omega(L_{gs}i_{sq} + L_m i_{rq}), \qquad (27)$$

$$v_{gq} = R_{gs}i_{sq} + L_{gs}\frac{di_{sq}}{dt} + L_m\frac{di_{rq}}{dt} + \omega(L_{gs}i_{sd} + L_m i_{rd}), \tag{28}$$

$$v_{rd} = R_r i_{rd} + L_r\frac{di_{rd}}{dt} + L_m\frac{di_{sd}}{dt} - \\ - (\omega - \omega_m)(L_r i_{rq} + L_m i_{sq}), \tag{29}$$

$$v_{rq} = R_r i_{rq} + L_r\frac{di_{rq}}{dt} + L_m\frac{di_{sq}}{dt} + \\ + (\omega - \omega_m)(L_r i_{rd} + L_m i_{sd}). \tag{30}$$

Therefore, four state variables are required to describe the dynamic behavior of the DFIG. In this case, the stator and rotor currents in the $d - q$ axes, i_{sd}, i_{sq}, i_{rd} and i_{rq}, are taken as state variables. By developing equations (27)-(30) the state equations of the system are obtained

$$\frac{di_{sd}}{dt} = \frac{1}{L_\sigma^2}[L_r R_{gs}i_{sd} + (L_m^2\omega_r - L_r L_{gs}\omega)i_{sq} - \\ - L_m R_r i_{rd} - L_m L_r \omega_m i_{rq} - L_r v_{gd} + L_m v_{rd}], \tag{31}$$

$$\frac{di_{sq}}{dt} = \frac{1}{L_\sigma^2}[-(L_m^2\omega_r - L_r L_{gs}\omega)]i_{sd} + L_r R_{gs}i_{sq} + \\ + L_m L_r \omega_m i_{rd} - L_m R_r i_{rq} - L_r v_{gq} + L_m v_{rq}], \tag{32}$$

$$\frac{di_{rd}}{dt} = \frac{1}{L_\sigma^2}[-L_m R_{gs}i_{sd} + L_m L_{gs}\omega_m i_{sq} + L_{gs}R_r i_{rd} + \\ + (L_m^2\omega - L_r L_{gs}\omega_r)i_{rq} + L_m v_{gd} - L_{gs}v_{rd}], \tag{33}$$

$$\frac{di_{rq}}{dt} = \frac{1}{L_\sigma^2}[-L_m L_{gs}\omega_m i_{sd} - L_m R_{gs}i_{sq} - \\ - (L_m^2\omega - L_r L_{gs}\omega_r)i_{rd} + L_{gs}R_r i_{rq} + \\ + L_m v_{gq} - L_{gs}v_{rq}], \tag{34}$$

where $L_\sigma^2 = L_m^2 - L_{gs}L_r$ and $\omega_r = \omega - \omega_m$.

The stator and rotor currents, and the stator voltage are taken as output of the model. The stator voltage can be deduced from the circuits of Fig. 7

$$v_{sd} = v_{gd} - R_g i_{sd} - L_g\frac{di_{sd}}{dt} + \omega L_g i_{sq}, \tag{35}$$

$$v_{sq} = v_{gq} - R_g i_{sq} - L_g\frac{di_{sq}}{dt} - \omega L_g i_{sd}. \tag{36}$$

The model inputs are the rotor and grid voltages in the $d-q$ axes, v_{rd}, v_{rq}, v_{gd} and v_{gq}. The grid voltage module, V_g, can be considered constant, but its projections in the $d-q$ axes are not, as they depend on the load angle δ which is defined as the angle between the voltage imposed by the RSC and the grid voltage. The grid frequency is assumed to be constant so the phase angle of the grid voltage, θ_g, varies linearly. However, since the rotor voltage is aligned with de d axis, the phase

angle of the rotor voltage varies according to the angle of the $d - q$ reference, θ, which is adjusted by the P-f control loop. Therefore, the load angle is variable. From Fig. 8 it is extracted that $v_{gd} = V_g cos\delta$ and $v_{gq} = V_g sin\delta$ where $\delta = \theta - \theta_g$. Likewise, the angular speed of the $d - q$ reference, ω, is an internal variable of the P-f control loop so it is not constant and, as a consequence, ω_r is not either.
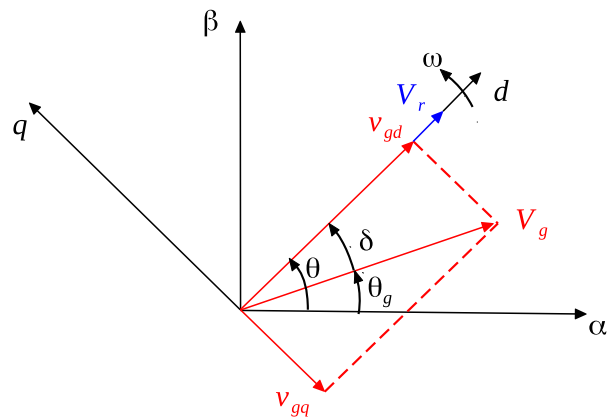

FIGURE 8. Rotor and grid voltages in the $d - q$ axes.

Therefore, the state and output equations are not linear. On the one hand, it is required to linearize the projections of the grid voltage in the $d - q$ axes, v_{gd} and v_{gq}, and, on the other hand, the crossed terms ωi_{xy} and $\omega_r i_{xy}$. For this purpose, a small-signal model is used. The currents are defined as the sum of the steady-state value and a small-signal perturbation,

$$i_{xy} = I_{xy0} + \Delta i_{xy},$$

where $x = s, r$ and $y = d, q$, and similarly the angular speed of the $d - q$ reference, ω, and the load angle, δ,

$$\omega = \omega_0 + \Delta\omega,$$

$$\delta = \delta_0 + \Delta\delta.$$

This way, nonlinear terms are linearized

$$\Delta v_{gd} = -V_g sin\delta_0\Delta\delta, \tag{37}$$

$$\Delta v_{gq} = V_g cos\delta_0\Delta\delta, \tag{38}$$

$$\Delta\omega i_{xy} = \omega_0\Delta i_{xy} + I_{xy0}\Delta\omega, \tag{39}$$

$$\Delta\omega_r i_{xy} = \omega_{r0}\Delta i_{xy} + I_{xy0}\Delta\omega, \tag{40}$$

and the linearized state equations are obtained

$$\frac{d\Delta i_{sd}}{dt} = \frac{1}{L_\sigma^2}[L_r R_{gs}\Delta i_{sd} + (L_m^2\omega_{r0} - L_r L_{gs}\omega_0)\Delta i_{sq} - \\ - L_m R_r\Delta i_{rd} - L_m L_r\omega_m\Delta i_{rq} + L_m\Delta v_{rd} + \\ + L_\sigma^2 I_{sq0}\Delta\omega + L_r V_g sin\delta_0\Delta\delta], \tag{41}$$

$$\frac{d\Delta i_{sq}}{dt} = \frac{1}{L_\sigma^2}[-(L_m^2\omega_{r0} - L_r L_{gs}\omega_0)\Delta i_{sd} + L_r R_{gs}\Delta i_{sq}+$$
$$+ L_m L_r \omega_m \Delta i_{rd} - L_m R_r \Delta i_{rq} + L_m \Delta v_{rq}-$$
$$- L_\sigma^2 I_{sd0}\Delta\omega - L_r V_g cos\delta_0\Delta\delta], \tag{42}$$

$$\frac{d\Delta i_{rd}}{dt} = \frac{1}{L_\sigma^2}[-L_m R_{gs}\Delta i_{sd} + L_m L_{gs}\omega_m \Delta i_{sq}+$$
$$+ L_{gs} R_r \Delta i_{rd} + (L_m^2\omega_0 - L_r L_{gs}\omega_{r0})\Delta i_{rq}-$$
$$- L_{gs}\Delta v_{rd} + L_\sigma^2 I_{rq0}\Delta\omega - L_m V_g sin\delta_0\Delta\delta], \tag{43}$$

$$\frac{d\Delta i_{rq}}{dt} = \frac{1}{L_\sigma^2}[-L_m L_{gs}\omega_m \Delta i_{sd} - L_m R_{gs}\Delta i_{sq}-$$
$$- (L_m^2\omega_0 - L_r L_{gs}\omega_{r0})\Delta i_{rd} + L_{gs} R_r \Delta i_{rq}-$$
$$- L_{gs}\Delta v_{rq} - L_\sigma^2 I_{rd0}\Delta\omega + L_m V_g cos\delta_0\Delta\delta]. \tag{44}$$

Likewise, linearizing (35) and (36) the following equations are obtained

$$\Delta v_{sd} = -L_g\frac{d\Delta i_{sd}}{dt} - R_g\Delta i_{sd} + L_g\Delta\omega i_{sq} - V_g sin\delta_0\Delta\delta, \tag{45}$$

$$\Delta v_{sq} = -L_g\frac{d\Delta i_{sq}}{dt} - R_g\Delta i_{sq} - L_g\Delta\omega i_{sd} + V_g cos\delta_0\Delta\delta. \tag{46}$$

Substituting (41) and (42) into (45) and (46), the linearized equations of the stator voltage are obtained

$$\Delta v_{sd} = -(\frac{L_g L_r}{L_\sigma^2}R_{gs} + R_g)\Delta i_{sd}+$$
$$+ [-\frac{L_g}{L_\sigma^2}(L_m^2\omega_{r0} - L_r L_{gs}\omega_0) + L_g\omega_0]\Delta i_{sq}+$$
$$+ \frac{L_g L_m R_r}{L_\sigma^2}\Delta i_{rd} + \frac{L_g L_m L_r \omega_m}{L_\sigma^2}\Delta i_{rq}-$$
$$- \frac{L_g L_m}{L_\sigma^2}\Delta v_{rd} - [(\frac{L_g L_r}{L_\sigma^2} + 1)V_g sin\delta_0]\Delta\delta, \tag{47}$$

$$\Delta v_{sq} = [\frac{L_g}{L_\sigma^2}(L_m^2\omega_{r0} - L_r L_{gs}\omega_0) - L_g\omega_0]\Delta i_{sd}-$$
$$- (\frac{L_g L_r}{L_\sigma^2}R_{gs} + R_g)\Delta i_{sq} - \frac{L_g L_m L_r \omega_m}{L_\sigma^2}\Delta i_{rd}+$$
$$+ \frac{L_g L_m R_r}{L_\sigma^2}\Delta i_{rq} - \frac{L_g L_m}{L_\sigma^2}\Delta v_{rq}+$$
$$+ [(\frac{L_g L_r}{L_\sigma^2} + 1)V_g cos\delta_0]\Delta\delta. \tag{48}$$

Equations (41)-(44), (47) and (48) define the linearized state-space model of the DFIG

$$\begin{pmatrix} \frac{d\Delta i_{sd}}{dt} \\ \frac{d\Delta i_{sq}}{dt} \\ \frac{d\Delta i_{rd}}{dt} \\ \frac{d\Delta i_{rq}}{dt} \end{pmatrix} = A\begin{pmatrix} \Delta i_{sd} \\ \Delta i_{sq} \\ \Delta i_{rd} \\ \Delta i_{rq} \end{pmatrix} + B\begin{pmatrix} \Delta v_{rd} \\ \Delta v_{rq} \\ \Delta\omega \\ \Delta\delta \end{pmatrix}, \tag{49}$$

$$\begin{pmatrix} \Delta i_{sd} \\ \Delta i_{sq} \\ \Delta i_{rd} \\ \Delta i_{rq} \\ \Delta v_{sd} \\ \Delta v_{sq} \end{pmatrix} = C\begin{pmatrix} \Delta i_{sd} \\ \Delta i_{sq} \\ \Delta i_{rd} \\ \Delta i_{rq} \end{pmatrix} + D\begin{pmatrix} \Delta v_{rd} \\ \Delta v_{rq} \\ \Delta\omega \\ \Delta\delta \end{pmatrix}, \tag{50}$$

where A, B, C, and D matrixes are defined in Appendix B.

B. RSC CONTROL

The current and voltage measurements are filtered by a low-pass analog filter, $LPAF = 1/(\tau s + 1)$, while the block D_{conv} as previously mentioned in III-A, models the delay due to digitization and for this purpose the first-order Padé approximation, (17), is used.

The control of the system is performed in the $d - q$ axes whose rotational speed ω is an internal variable of the control itself. Therefore, the control is performed in a variable speed rotating reference frame and all control elements must be referenced to that reference frame. To rotate the transfer functions between the different references, the transformation presented in [42] is used. In equilibrium, the rotational speed of the $d - q$ axes coincides with the grid frequency, $\omega = \omega_0$. For simplicity, to perform the transformations from $LPAF$ and D_{conv} to $d-q$, variations of ω are neglected and the $d - q$ axes are considered to rotate at ω_0 as the small-signal perturbation, $\Delta\omega$, has slight influence in these modes. For example, considering the $LPAF$ defined in a stationary reference frame, its equivalent model in the $d - q$ axes is a 2x2 MIMO model

$$[LPAF]_\omega = \frac{1}{2}\begin{bmatrix} LPAF_1(s) & LPAF_2(s) \\ -LPAF_2(s) & LPAF_1(s) \end{bmatrix}, \tag{51}$$

where $LPAF_1(s) = LPAF(s + j\omega) + LPAF(s - j\omega)$ and $LPAF_2(s) = jLPAF(s + j\omega) - jLPAF(s - j\omega)$. In the stator, since the $LPAF$ is defined in a stationary reference frame with the stator, $\alpha\beta_s$, the rotation is performed with ω_0, $[LPAF]_{\omega_0}$. In contrast, for the RSC, $[D_{conv}]$ is defined in a stationary reference frame with the rotor windings, $\alpha\beta_m$, which rotates at ω_m, so the transformation is performed with ω_r, $[D_{conv}]_{\omega_r}$.

C. POWER CALCULATION

To determine the stator active and reactive powers the filtered measurements of the stator voltages and currents are used. The generated powers can be computed as

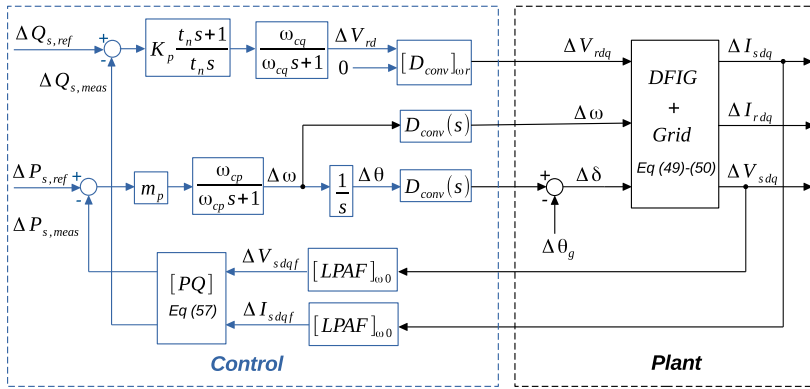$$P_{s,meas} = -(v_{sdf}i_{sdf} + v_{sqf}i_{sqf}), \tag{52}$$

8

IEEE*Access*

FIGURE 9. Proposed model block diagram.

$$Q_{s,meas} = -(v_{sqf}i_{sdf} - v_{sdf}i_{sqf}). \tag{53}$$

In the model developed in IV-A a motor convention is assumed, so to determine the generated powers in (52) and (53) a negative sign is introduced.

The power equations are not linear, so a small-signal model is used to linearize these expressions. Defining stator voltages and currents as

$$v_{syf} = V_{syf0} + \Delta v_{syf},$$

$$i_{syf} = I_{syf0} + \Delta i_{syf},$$

where $y = d, q$, the linearized power expressions are obtained

$$\Delta P_{s,meas} = -I_{sdf0}\Delta v_{sdf} - I_{sqf0}\Delta v_{sqf} - V_{sdf0}\Delta i_{sdf} - \\ - V_{sqf0}\Delta i_{sqf}, \tag{54}$$

$$\Delta Q_{s,meas} = I_{sqf0}\Delta v_{sdf} - I_{sdf0}\Delta v_{sqf} - V_{sqf0}\Delta i_{sdf} + \\ + V_{sdf0}\Delta i_{sqf}. \tag{55}$$

Equations (54) and (55) can be expressed in matrix form as

$$\begin{pmatrix} \Delta P_{s,meas} \\ \Delta Q_{s,meas} \end{pmatrix} = [PQ] \begin{pmatrix} \Delta v_{sdf} \\ \Delta v_{sqf} \\ \Delta i_{sdf} \\ \Delta i_{sqf} \end{pmatrix}, \tag{56}$$

where

$$[PQ] = \begin{bmatrix} -I_{sdf0} & -I_{sqf0} & -V_{sdf0} & -V_{sqf0} \\ I_{sqf0} & -I_{sdf0} & -V_{sqf0} & V_{sdf0} \end{bmatrix}. \tag{57}$$

Finally, in Fig. 9 the complete proposed model is represented in block diagram form.

V. VALIDATION OF THE PROPOSED MODEL BY SIMULATION

To validate the linearized small-signal model proposed in IV, its stability and dynamic response is compared to the stability range and step-response of the model built in MAT-LAB/Simulink. The stability range of the Simulink model has been previously determined in III-B by analyzing its step-response, and the results obtained are plotted in the first column of Fig. 10.
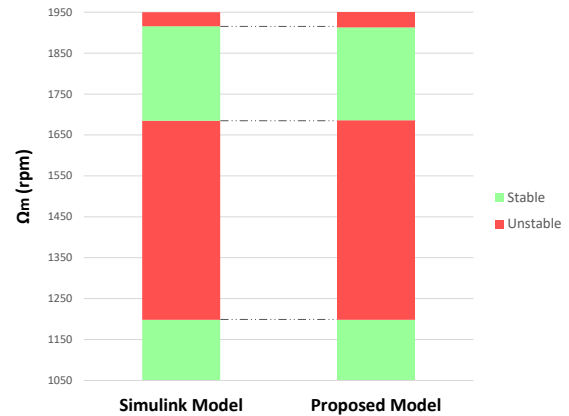

FIGURE 10. Simulink and proposed model stability comparison.

The stability range of the proposed model is determined in MATLAB by analyzing the position of the closed-loop poles. First, the model has been linearized for an active reference power equal to the nominal power, 2 MW, and a null reactive power. Then, in the operating speed range of the machine (from 1050 to 1950 rpm) the closed-loop poles of the system have been obtained. In Fig. 11 the evolution of the closed-loop poles as a function the machine's rotational speed is represented. The poles corresponding to operating points below synchronism are represented in blue and the poles corresponding to operating points above synchronism in red. Thus, the stability range of the proposed model has been determined (see second column of Fig. 10).
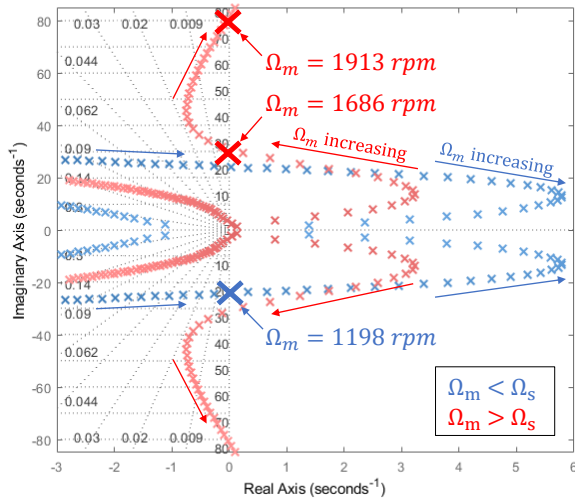
FIGURE 11. Evolution of the closed-loop poles of the proposed model as a function of rotational speed.
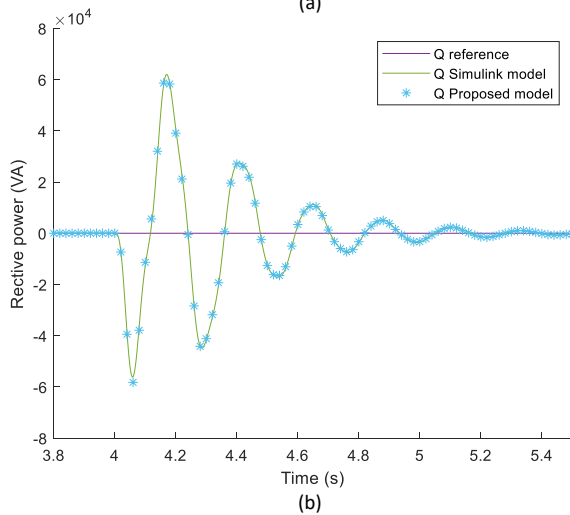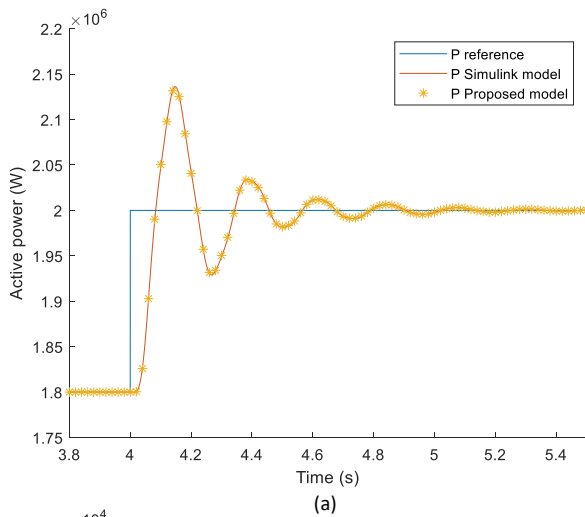

FIGURE 12. Step-response of Simulink and proposed model at Ω_m=1050 rpm: (a) active power and (b) reactive power.
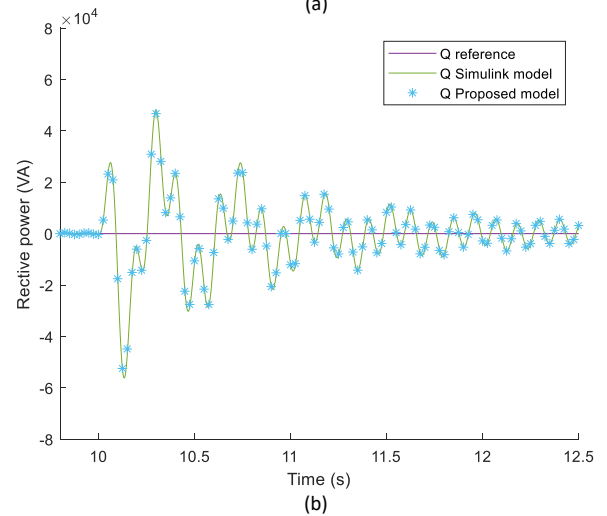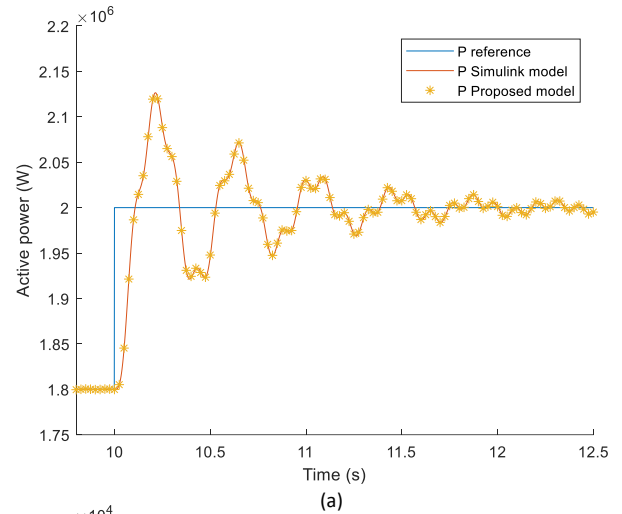

FIGURE 13. Step-response of Simulink and proposed model at Ω_m=1800 rpm: (a) active power and (b) reactive power.

As can be seen in Fig. 10 the stability range of the models coincides. Below synchronism both models are stable from 1050 to 1198 rpm, and above synchronism the stability range is almost equal; the Simulink model is stable from 1686 to 1917 rpm and the proposed model from 1687 to 1913 rpm.

Once it has been verified that the stability range of the models coincides, their dynamic response is compared. A step from 1.8 MW to 2 MW has been introduced in the reference active power, keeping the reference reactive power at zero, and the evolution of both active and reactive powers has been analyzed. Fig. 12 and Fig. 13 show the simulation results at 1050 rpm and 1800 rpm, and as can be seen, the proposed model exhibit an identical dynamic response to that of the Simulink model. These simulation results validate the proposed model, so it could be used to adjust stable controllers for all possible operating points of droop-controlled DFIG wind turbines.

IEEE *Access*

VI. CONCLUSION

This paper presents a linearized small-signal model that accurately represents the stability and dynamic response of a droop-controlled DFIG wind turbine. Traditionally, to characterize the response of droop-controlled systems RMS models have been used. However, those models are not suitable for DFIG wind turbines, as it is verified in this paper. The proposed model, unlike the models developed in previous works, models the internal dynamics of the machine taking into account all the nonlinearities that the system presents due to its interaction with the control. To validate the proposed model its stability and step-response is compared with that of the model built in MATLAB/Simulink. The simulation results show that the proposed model allows to analyze the stability and reproduce the dynamic response of the system under study with high accuracy. The following work will focus on adjusting the control to stabilize the response of the system over the whole range of rotational speeds of the machine and for different reference active and reactive powers.

.

APPENDIX A SYSTEM PARAMETERS

TABLE 1. System Parameters (referred to the stator)

Parameter	Magnitude
Grid	
$S_B = 2\,MVA, U = 690\,V, f_g = 50\,Hz$	
Line reactance (L_g)	0.1 p.u.
Line resistance (R_g)	0.015 p.u.
DFIG	
$S = 2\,MVA, U = 690\,V, f_{gen} = 50\,Hz$	
Rotor resistance (R_r)	$0.0018\,\Omega$
Rotor leakage inductance (L_{lr})	$76.3\,\mu H$
Stator resistance (R_s)	$0.0032\,\Omega$
Stator leakage inductance (L_{ls})	$161\,\mu H$
Mutual inductance (L_m)	$0.0025\,H$
Pole pairs (pp)	2
Power converter	
Sampling frequency	5.7 kHz
Control parameters	
P-f droop coefficient (m_p)	0.05 p.u.
Q-V PI proportional gain (K_p)	0.33 abs(s) p.u.
Q-V PI integral time constant (t_n)	0.01
P-f loop low-pass filter cut-off frequency (ω_{cp})	abs(ω_r)/10 rad/s
Q-V loop low-pass filter cut-off frequency (ω_{cq})	abs(ω_r)/10 rad/s
Low-pass analog filter time constant (τ)	1.061^{-4}
References for the simulations	
Active power initial reference ($P_{s,ref,0}$)	1.8 MW
Active power final reference ($P_{s,ref,f}$)	2 MW
Reactive power reference ($Q_{s,ref}$)	0 MVA
Angular frequency (ω_{ref})	$2\pi 50$ rad/s
Voltage reference ($V_{r,ref}$)	690 abs(s) V

APPENDIX B DFIG AND GRID MODEL

$$A = \frac{1}{L_\sigma^2} \begin{bmatrix} A_{11} & A_{12} \\ A_{21} & A_{22} \end{bmatrix} \tag{58}$$

where

$$A_{11} = \begin{bmatrix} L_r R_{gs} & L_m^2 \omega_{r0} - L_r L_{gs} \omega_0 \\ -(L_m^2 \omega_{r0} - L_r L_{gs} \omega_0) & L_r R_{gs} \end{bmatrix} \tag{59}$$

$$A_{12} = \begin{bmatrix} -L_m R_r & -L_m L_r \omega_m \\ L_m L_r \omega_m & -L_m R_r \end{bmatrix} \tag{60}$$

$$A_{21} = \begin{bmatrix} -L_m R_{gs} & L_m L_{gs} \omega_m \\ -L_m L_{gs} \omega_m & -L_m R_{gs} \end{bmatrix} \tag{61}$$

$$A_{22} = \begin{bmatrix} L_{gs} R_r & L_m^2 \omega_0 - L_r L_{gs} \omega_{r0} \\ -(L_m^2 \omega_0 - L_r L_{gs} \omega_{r0}) & L_{gs} R_r \end{bmatrix} \tag{62}$$

$$B = \frac{1}{L_\sigma^2} \begin{bmatrix} L_m & 0 & L_\sigma^2 I_{sq0} & L_r V_g sin\delta_0 \\ 0 & L_m & -L_\sigma^2 I_{sd0} & -L_r V_g cos\delta_0 \\ -L_{gs} & 0 & L_\sigma^2 I_{rq0} & -L_m V_g sin\delta_0 \\ 0 & -L_{gs} & -L_\sigma^2 I_{rd0} & L_m V_g cos\delta_0 \end{bmatrix} \tag{63}$$

$$C = \begin{bmatrix} 1 & 0 & 0 & 0 \\ 0 & 1 & 0 & 0 \\ 0 & 0 & 1 & 0 \\ 0 & 0 & 0 & 1 \\ C_{21} & C_{22} & C_{23} & C_{24} \end{bmatrix} \tag{64}$$

where

$$C_{21} = \begin{bmatrix} -(\frac{L_g L_r}{L_\sigma^2} R_{gs} + R_g) \\ \frac{L_g}{L_\sigma^2}(L_m^2 \omega_{r0} - L_r L_{gs} \omega_0) - L_g \omega_0 \end{bmatrix} \tag{65}$$

$$C_{22} = \begin{bmatrix} -\frac{L_g}{L_\sigma^2}(L_m^2 \omega_{r0} - L_r L_{gs} \omega_0) + L_g \omega_0 \\ -(\frac{L_g L_r}{L_\sigma^2} R_{gs} + R_g) \end{bmatrix} \tag{66}$$

$$C_{23} = \begin{bmatrix} \frac{L_g L_m R_r}{L_\sigma^2} \\ -\frac{L_g L_m L_r \omega_m}{L_\sigma^2} \end{bmatrix} \tag{67}$$

$$C_{24} = \begin{bmatrix} \frac{L_g L_m L_r \omega_m}{L_\sigma^2} \\ \frac{L_g L_m R_r}{L_\sigma^2} \end{bmatrix} \tag{68}$$

$$D = \begin{bmatrix} 0 & 0 & 0 & 0 \\ 0 & 0 & 0 & 0 \\ 0 & 0 & 0 & 0 \\ 0 & 0 & 0 & 0 \\ -\frac{L_g L_m}{L_\sigma^2} & 0 & 0 & -(\frac{L_g L_r}{L_\sigma^2} + 1)V_g sin\delta_0 \\ 0 & -\frac{L_g L_m}{L_\sigma^2} & 0 & (\frac{L_g L_r}{L_\sigma^2} + 1)V_g cos\delta_0 \end{bmatrix} \tag{69}$$

REFERENCES

[1] T. Telsnig, "Wind energy technology development report 2020," 02 2021.

[2] R. Rosso, X. Wang, M. Liserre, X. Lu, and S. Engelken, "Grid-forming converters: Control approaches, grid-synchronization, and future trends—a review," *IEEE Open Journal of Industry Applications*, vol. 2, pp. 93–109, 2021.

[3] K. V. Kkuni, S. Mohan, G. Yang, and W. Xu, "Comparative assessment of typical controlrealizations of grid forming converters based ontheir voltage source behaviour," 2021.

[4] J. M. Guerrero, J. C. Vasquez, J. Matas, L. G. de Vicuna, and M. Castilla, "Hierarchical control of droop-controlled ac and dc microgrids—a general approach toward standardization," *IEEE Transactions on Industrial Electronics*, vol. 58, no. 1, pp. 158–172, 2011.

[5] J. Rocabert, A. Luna, F. Blaabjerg, and P. Rodríguez, "Control of power converters in ac microgrids," *IEEE Transactions on Power Electronics*, vol. 27, no. 11, pp. 4734–4749, 2012.

[6] H.-P. Beck and R. Hesse, "Virtual synchronous machine," in *2007 9th International Conference on Electrical Power Quality and Utilisation*, 2007, pp. 1–6.

[7] S. D'Arco and J. A. Suul, "Virtual synchronous machines — classification of implementations and analysis of equivalence to droop controllers for microgrids," in *2013 IEEE Grenoble Conference*, 2013, pp. 1–7.

[8] C. Arghir, T. Jouini, and F. Dörfler, "Grid-forming control for power converters based on matching of synchronous machines," *Automatica*, vol. 95, pp. 273–282, 2018. [Online]. Available: https://www.sciencedirect.com/science/article/pii/S0005109818302796

[9] B. B. Johnson, S. V. Dhople, A. O. Hamadeh, and P. T. Krein, "Synchronization of parallel single-phase inverters with virtual oscillator control," *IEEE Transactions on Power Electronics*, vol. 29, no. 11, pp. 6124–6138, 2014.

[10] B. B. Johnson, M. Sinha, N. G. Ainsworth, F. Dörfler, and S. V. Dhople, "Synthesizing virtual oscillators to control islanded inverters," *IEEE Transactions on Power Electronics*, vol. 31, no. 8, pp. 6002–6015, 2016.

[11] M. Colombino, D. Groß, J.-S. Brouillon, and F. Dörfler, "Global phase and magnitude synchronization of coupled oscillators with application to the control of grid-forming power inverters," *IEEE Transactions on Automatic Control*, vol. 64, no. 11, pp. 4496–4511, 2019.

[12] D. Groß, M. Colombino, J.-S. Brouillon, and F. Dörfler, "The effect of transmission-line dynamics on grid-forming dispatchable virtual oscillator control," *IEEE Transactions on Control of Network Systems*, vol. 6, no. 3, pp. 1148–1160, 2019.

[13] K. De Brabandere, B. Bolsens, J. Van den Keybus, A. Woyte, J. Driesen, and R. Belmans, "A voltage and frequency droop control method for parallel inverters," *IEEE Transactions on Power Electronics*, vol. 22, no. 4, pp. 1107–1115, 2007.

[14] Y. A.-R. I. Mohamed and E. F. El-Saadany, "Adaptive decentralized droop controller to preserve power sharing stability of paralleled inverters in distributed generation microgrids," *IEEE Transactions on Power Electronics*, vol. 23, no. 6, pp. 2806–2816, 2008.

[15] L. Zhang, L. Harnefors, and H.-P. Nee, "Power-synchronization control of grid-connected voltage-source converters," *IEEE Transactions on Power Systems*, vol. 25, no. 2, pp. 809–820, 2010.

[16] M. Chandorkar, D. Divan, and R. Adapa, "Control of parallel connected inverters in standalone ac supply systems," *IEEE Transactions on Industry Applications*, vol. 29, no. 1, pp. 136–143, 1993.

[17] T. Qoria, T. Prevost, G. Denis, F. Gruson, F. Colas, and X. Guillaud, "Power converters classification and characterization in power transmission systems," in *2019 21st European Conference on Power Electronics and Applications (EPE '19 ECCE Europe)*, 2019, pp. P.1–P.9.

[18] M. A. Abusara, S. M. Sharkh, and J. M. Guerrero, "Improved droop control strategy for grid-connected inverters," *Sustainable Energy, Grids and Networks*, vol. 1, pp. 10–19, 2015. [Online]. Available: https://www.sciencedirect.com/science/article/pii/S2352467714000034

[19] T. Qoria, Q. Cossart, C. Li, X. Guillaud, F. Colas, F. Gruson, and X. Kestelyn, "Deliverable 3.2: Local control and simulation tools for large transmission systems," MIGRATE project, Report, 2018. [Online]. Available: https://www.h2020-migrate.eu/downloads.html

[20] T. Qoria, F. Gruson, F. Colas, X. Guillaud, M.-S. Debry, and T. Prevost, "Tuning of cascaded controllers for robust grid-forming voltage source converter," in *2018 Power Systems Computation Conference (PSCC)*, 2018, pp. 1–7.

[21] B. Liu, J. Liu, Z. Liu, T. Wu, and R. An, "An accurate power control scheme for droop-controlled grid-connected inverters," in *2018 IEEE Applied Power Electronics Conference and Exposition (APEC)*, 2018, pp. 2374–2378.

[22] B. Liu, J. Liu, and Z. Liu, "Improvement of grid current quality for droop-controlled grid-connected inverters under distorted grid conditions," in *2019 IEEE Energy Conversion Congress and Exposition (ECCE)*, 2019, pp. 2560–2565.

[23] X. Meng, J. Liu, and Z. Liu, "A generalized droop control for grid-supporting inverter based on comparison between traditional droop control and virtual synchronous generator control," *IEEE Transactions on Power Electronics*, vol. 34, no. 6, pp. 5416–5438, 2019.

[24] T. Qoria, F. Gruson, F. Colas, G. Denis, T. Prevost, and X. Guillaud, "Inertia effect and load sharing capability of grid forming converters connected to a transmission grid," in *15th IET International Conference on AC and DC Power Transmission (ACDC 2019)*, 2019, pp. 1–6.

[25] D. Pérez-Estévez, J. Doval-Gandoy, and J. M. Guerrero, "Ac-voltage harmonic control for stand-alone and weak-grid-tied converter," *IEEE Transactions on Industry Applications*, vol. 56, no. 1, pp. 403–421, 2020.

[26] W. Du, Z. Chen, K. P. Schneider, R. H. Lasseter, S. Pushpak Nandanoori, F. K. Tuffner, and S. Kundu, "A comparative study of two widely used grid-forming droop controls on microgrid small-signal stability," *IEEE Journal of Emerging and Selected Topics in Power Electronics*, vol. 8, no. 2, pp. 963–975, 2020.

[27] M. G. Taul, X. Wang, P. Davari, and F. Blaabjerg, "Current limiting control with enhanced dynamics of grid-forming converters during fault conditions," *IEEE Journal of Emerging and Selected Topics in Power Electronics*, vol. 8, no. 2, pp. 1062–1073, 2020.

[28] M. Amelian, R. Hooshmand, A. Khodabakhshian, and H. Saberi, "Small signal stability improvement of a wind turbine-based doubly fed induction generator in a microgrid environment," in *ICCKE 2013*, 2013, pp. 384–389.

[29] M. Marhaba, S. Farhangi, H. Imaneini, and R. Iravani, "Reactive power sharing improvement of droop-controlled dfig wind turbines in a microgrid," *IET Generation, Transmission & Distribution*, vol. 12, 10 2017.

[30] M. F. M. Arani and Y. A.-R. I. Mohamed, "Analysis and impacts of implementing droop control in dfig-based wind turbines on microgrid/weak-grid stability," *IEEE Transactions on Power Systems*, vol. 30, no. 1, pp. 385–396, 2015.

[31] R. K. Rastogi and R. Sharma, "Improved synchronization and voltage regulation of dfig based wind energy system (wes)," in *2018 International Conference on Current Trends towards Converging Technologies (ICCTCT)*, 2018, pp. 1–5.

[32] J. A. Cortajarena, J. De Marcos, P. Alkorta, O. Barambones, and J. Cortajarena, "Dfig wind turbine grid connected for frequency and amplitude control in a smart grid," in *2018 IEEE International Conference on Industrial Electronics for Sustainable Energy Systems (IESES)*, 2018, pp. 362–369.

[33] Y. Han and J.-I. Ha, "Droop control using impedance of grid-integrated dfig within microgrid," *IEEE Transactions on Energy Conversion*, vol. 34, no. 1, pp. 88–97, 2019.

[34] S. A. Eisa, "Modeling dynamics and control of type-3 dfig wind turbines: Stability, q droop function, control limits and extreme scenarios simulation," *Electric Power Systems Research*, vol. 166, pp. 29–42, 2019. [Online]. Available: https://www.sciencedirect.com/science/article/pii/S0378779618303110

[35] H. Xiao, Z. Zhao, K. Zhou, J. Guo, C. S. Lai, and L. Lei Lai, "Voltage-source control of dfig in standalone wind power-based microgrids," in *2020 IEEE 1st China International Youth Conference on Electrical Engineering (CIYCEE)*, 2020, pp. 1–7.

[36] U. Datta, A. Kalam, and J. Shi, "Frequency performance analysis of multi-gain droop controlled dfig in an isolated microgrid using real-time digital simulator," *Engineering Science and Technology, an International Journal*, vol. 23, no. 5, pp. 1028–1041, 2020. [Online]. Available: https://www.sciencedirect.com/science/article/pii/S2215098619318014

[37] Z. Xie, X. Gao, S. Yang, and X. Zhang, "Improved fractional-order damping method for voltage-controlled dfig system under weak grid," *Journal of Modern Power Systems and Clean Energy*, pp. 1–10, 2021.

[38] Y. Jiao and H. Nian, "Grid-forming control for dfig based wind farms to enhance the stability of lcc-hvdc," *IEEE Access*, vol. 8, pp. 156 752–156 762, 2020.

[39] J. L. Agorreta, M. Borrega, J. López, and L. Marroyo, "Modeling and control of n-paralleled grid-connected inverters with lcl filter coupled due to grid impedance in pv plants," *IEEE Transactions on Power Electronics*, vol. 26, no. 3, pp. 770–785, 2011.

[40] P. C. Krause, O. Wasynczuk, and S. D. Sudhoff, *Analysis of electric machinery and drive systems*. IEEE Press, 2002.

[41] N. Mohan, T. M. Undeland, and W. P. Robbins, *Power Electronics: Converters, Applications, and Design*. John Wiley & Sons, Inc., 1995.

[42] D. Zmood, D. Holmes, and G. Bode, "Frequency-domain analysis of three-phase linear current regulators," *IEEE Transactions on Industry Applications*, vol. 37, no. 2, pp. 601–610, 2001.

EUGENIO GUBIA (M'04) received the M.Sc. and Ph.D. degrees in industrial engineering from the Public University of Navarre, Spain, in 1995 and 2003, respectively.

He joined the Electrical and Electronic Department of the Public University of Navarre in 1996, where he is currently an associate professor and member of the Institute of Smart Cities (ISC). In 2002, he joined the Electrical Engineering, Power Electronics, and Renewable Energy Research Group (INGEPER). From June to December 2005, he worked as a guest researcher at the Center for Power Electronics Systems (CPES) in the field of electromagnetic compatibility. His research interests are in the field of power electronics, renewable energy systems, high-frequency phenomena, and electromagnetic compatibility.

IKER ORAA was born in Pamplona, Spain, in 1996. He received the B.Sc. and the M.Sc. degree in industrial engineering, in 2018 and 2020, respectively, from the Public University of Navarre (UPNA), Pamplona, Spain.

In 2020, he joined the Electrical Engineering, Power Electronics and Renewable Energy Research Group (INGEPER), UPNA. His research interests include renewable energies and control of power electronics.

JAVIER SAMANES (S'15 - M'18) was born in Pamplona, Spain, in 1990. He received the M.Sc. degree in electrical engineering from the Public University of Navarre (UPNA), Pamplona, Spain, in 2014 and the M.Sc. degree in renewable energy engineering in 2016 from the same institution. He obtained the Ph.D. degree in electrical engineering from the UPNA in 2018.

In 2014, he joined the Electrical Engineering, Power Electronics and Renewable Energy Research Group (INGEPER) at the UPNA, where he is currently Assistant Professor and member of the Institute of Smart Cities (ISC). In 2018 he was visiting scholar in the Center for Power Electronic Systems (CPES) at Virginia Tech, USA. His research interests include power electronics and renewable energies.

JESUS LOPEZ (M'05) was born in Pamplona, Spain, in 1975. He received the M.Sc. degree in industrial engineering from the Public University of Navarra, Pamplona, Spain, in 2000. In 2008 he received the Ph.D. degree in industrial engineering from the Public University of Navarra, Spain, in collaboration with the LAPLACE laboratory, Toulouse, France.

In 2001, he joined the Power Electronic Group, Electrical and Electronic Department at the Public University of Navarra, where he is currently an Assistant Professor and is also involved in research projects mainly in co-operation with industry. His research interests are in the field of power electronics, power systems quality and renewable energies, such as wind turbines and photovoltaic plants.